

Dynamic strain modulation of a nanowire quantum dot compatible with a thin-film lithium niobate photonic platform

Thomas Descamps,^{1,*} Tanguy Schetelat,¹ Jun Gao,¹ Philip J. Poole,² Dan Dalacu,² Ali W. Elshaari,¹ and Val Zwiller^{1,3,†}

¹*Department of Applied Physics, KTH Royal Institute of Technology, Roslagstullsbacken 21, 10691 Stockholm, Sweden*

²*National Research Council of Canada, Ottawa, Ontario K1A 0R6, Canada*

³*Single Quantum BV, Delft, The Netherlands*

(Dated: June 12, 2023)

The integration of on-demand single photon sources in photonic circuits is a major prerequisite for on-chip quantum applications. Among the various high-quality sources, nanowire quantum dots can be efficiently coupled to optical waveguides because of their preferred emission direction along their growth direction. However, local tuning of the emission properties remains challenging. In this work, we transfer a nanowire quantum dot on a bulk lithium niobate substrate and show that its emission can be dynamically tuned by acousto-optical coupling with surface acoustic waves. The purity of the single photon source is preserved during the strain modulation. We further demonstrate that the transduction is maintained even with a SiO₂ encapsulation layer deposited on top of the nanowire acting as the cladding of a photonic circuit. Based on these experimental findings and numerical simulations, we introduce a device architecture consisting of a nanowire quantum dot efficiently coupled to a thin film lithium niobate rib waveguide and strain-tunable by surface acoustic waves.

Quantum computation with on-chip photonic qubits has emerged as an important research area in quantum technologies [1–4]. In addition to the manipulation and detection of individual photons, achieving deterministic integration of high-purity, on-demand single photon sources is essential for the scalability and complexity of quantum photonic circuits [5–7]. Although more technologically challenging than monolithic approaches [8, 9], the heterogeneous integration of high-quality quantum emitters offers the possibility of producing more efficient devices and incorporating additional functionalities that would be difficult to achieve in single material systems. Towards this direction, III/V semiconductor quantum dots (QDs) [10–14], and defects in crystals [15, 16] or in 2D materials [17–19] have been successfully transferred to Si, SiN, AlN or LiNbO₃ while maintaining good performance as single photon sources. Yet, tuning of the source emission properties remains a challenge and would require an external electric [20], magnetic [21] or strain field [22, 23] specifically applied to the source. Surface acoustic waves (SAWs), generated from a piezoelectric material by an interdigital transducer (IDT), can interact with a large variety of quantum systems. Coupling to superconducting qubits [24, 25], coherent electron transport between gate-defined QDs [26] as well as coherent acoustic control of optically active QDs [27, 28] have been demonstrated. In the latter case, the piezoelectric potential generated by the SAW can be used to transport photo-generated carriers to the QD [29], while the QD bandgap can also be modulated by the in-plane strain field of the SAW [30–33].

Among the various transferable emitters or defects, InAsP QDs embedded in an InP nanowire (NW) with

a taper-shaped InP shell stands out as a good candidate [34, 35]. Bright [36], high-purity [37], near transform-limited [38] and indistinguishable single photons as well as entangled photons pairs [39, 40] have been preferentially emitted along the long axis of the NW with a Gaussian transverse mode. This emission profile is advantageous for efficient coupling to single mode waveguides and fibers. Site-controlled growth with high yield [41] is also particularly convenient for deterministic integration on photonic chips using pick-and-place techniques. On-chip routing, filtering, tuning, multiplexing and detection of emitted single photons has been demonstrated on a SiN platform [13, 14, 42–44].

In this work, we demonstrate the modulation of a single tapered QD NW with surface acoustic waves. The NW was transferred to a bulk LiNbO₃ substrate and bonded to the substrate by Van der Waals interactions. LiNbO₃ offers a large electromechanical coupling coefficient ($k^2 \approx 5\%$) making it particularly suited to modulate the emission of QDs at moderate RF power [45]. We show that the emission wavelength of the quantum emitter can be tuned by more than 1 nm at the SAW resonance frequency while the single photon purity is preserved. We then explore the influence of a SiO₂ encapsulation layer on the strain tuning performance. On the one side, this layer rigidly anchors the NW to the substrate, making it easier to manufacture a photonic chip if the NW is first transferred onto an unprocessed substrate. On the other side, once the NW is placed on the photonic waveguide, the SiO₂ layer acts as a cladding layer. Based on these findings, we propose a device architecture where the NW is adiabatically coupled to a rib waveguide made from a LiNbO₃ thin film and compatible with SAW-induced strain modulation. This fully integrated strain-tunable source will open the way for further on-chip manipulation and detection of photonic qubits.

The chip consists of two IDTs forming a 200 μm delay

* descamps@kth.se

† zwiller@kth.se

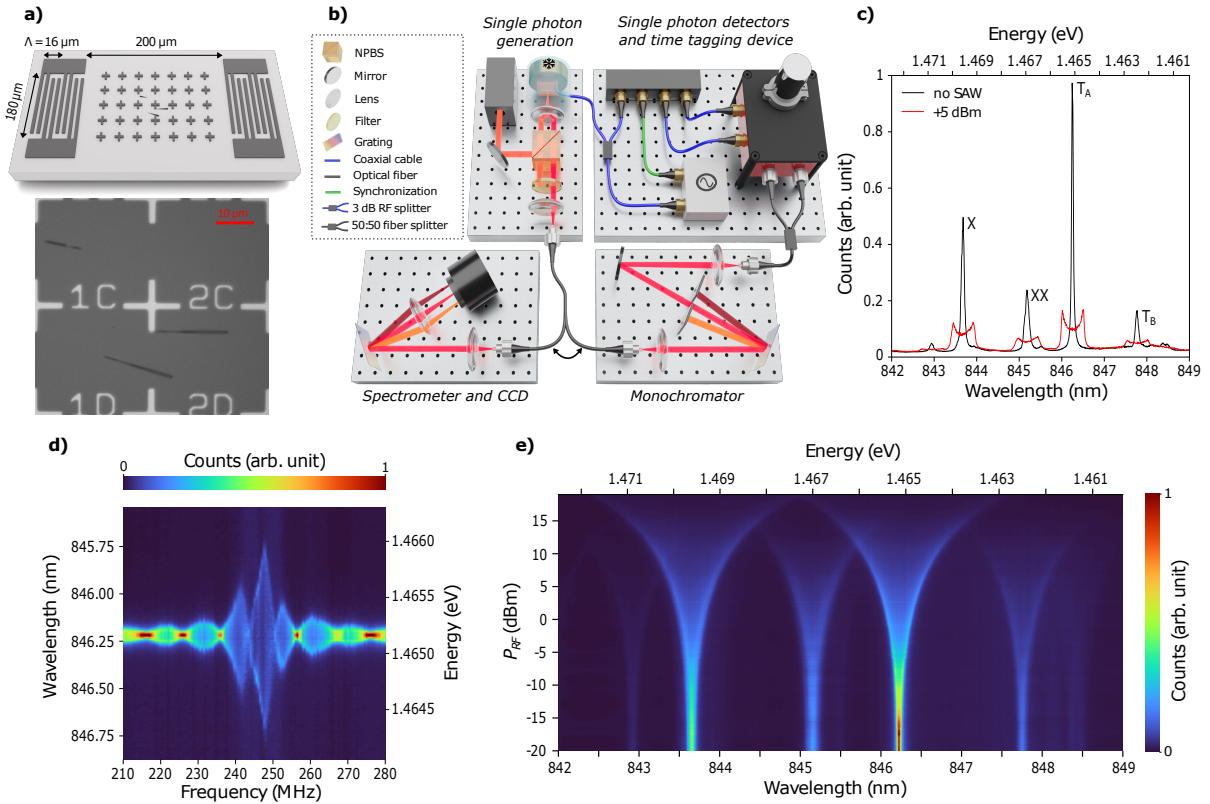


FIG. 1. a) Sketch of the surface acoustic wave delay line with an optical microscope image of individually transferred nanowires. b) Optical setup for spectroscopy or time-resolved measurement (NPBS: non-polarizing beam splitter). c) Emission peaks of the nanowire QD without (black) and with (red) the SAW-induced modulation ($P_{RF} = 5 \text{ dBm}$ at 247.5 MHz). d) Optical modulation of line T_A around the fundamental resonance frequency of the IDT ($P_{RF} = 10 \text{ dBm}$). e) Optical modulation as a function of P_{RF} (SAW generation at 247.5 MHz). For all measurements, the QD was continuously excited with a He-Ne laser at 150 nW .

line patterned on a 128° Y-X cut LiNbO_3 substrate by optical lithography and etching of a 60 nm -thick chromium layer (Fig. 1(a)). The IDTs have a double-electrode structure to avoid internal reflections of the SAW [46]. The electrodes are $2 \mu\text{m}$ wide, resulting in a spatial period $\Lambda = 16 \mu\text{m}$ repeated 25 times per IDT. This configuration gives two SAW excitation frequencies, one fundamental resonance at $f_1 = c_s/\Lambda = 249 \text{ MHz}$ and a third harmonic at $f_3 = 3c_s/\Lambda = 748 \text{ MHz}$ where c_s is the speed of sound in the substrate ($c_{\text{LiNbO}_3} = 3990 \text{ ms}^{-1}$). The site-controlled InP NW embedding the InAsP QD was individually picked up with a micro-manipulator and transferred onto the LiNbO_3 chip within the delay line. The long axis of the NW is approximately parallel to the direction of propagation of the acoustic wave. In the following measurements, only the fundamental resonance is investigated. The sample was investigated at 1.8 K in a dry cryostat designed for confocal micro-photoluminescence (PL) measurements and equipped with high frequency cables (Fig. 1(b)). A continuous wave He-Ne laser was focused with a microscope objective to excite the QD above band. The collected PL was dispersed by a 750 cm focal length spectrometer and detected by a liquid nitrogen-cooled charge-coupled device (CCD) camera. An ana-

log signal generator was used to apply a sinusoidal radio frequency (RF) signal of adjustable power P_{RF} to one IDT of the delay line while the other was floating. Fig. 1(c) shows the PL spectrum of the QD without applying SAWs. From higher to lower energy, the four peaks are identified as the exciton X, the biexciton XX and two trions T_A and T_B based on power-dependent measurements (see Supporting Information Fig. S1) [47] and previous studies [39].

When a RF signal is applied to the IDT, the radiated SAW couples to the QD through its strain field. Since the QD size is smaller by approximately three orders of magnitude than the wavelength Λ of the SAW, the strain field experienced by the QD can be considered uniformly distributed. The sinusoidal modulation of the strain field causes a modulation of the bandgap of the QD at the same frequency, resulting in the oscillation of the spectral lines around their unstrained energies. The time average of this oscillation gives a broad spectral line with peaks at the edges, as plotted in Fig. 1(c) for a $P_{RF} = 5 \text{ dBm}$ sinusoidal signal at 247.5 MHz . For a given RF power, the tuning magnitude is largest when the SAW is generated close to the resonance frequency f_1 of the IDT, as shown in Fig. 1(d) for

the T_A line. The main resonance peak is centered around 247.5 MHz, which corresponds to an effective speed of sound in LiNbO_3 of $c_{\text{LiNbO}_3, \text{eff}} = 3960 \text{ ms}^{-1}$. This main resonance spanning 20 MHz is split into three lobes separated by $\delta f = 6.6 \text{ MHz}$ since the delay line behaves as an acoustic cavity. The effective length of the cavity is hence $c_{\text{LiNbO}_3, \text{eff}}/2\delta f \simeq 300 \mu\text{m}$ which is slightly larger than the physical length of the delay line due to the penetration of the SAW inside the two IDTs. A similar response is obtained for all the other lines of the QD. At the SAW resonance frequency, detuning becomes observable for all the peaks around $P_{RF} = -15 \text{ dBm}$ and can reach up to 1.5 nm at 15 dBm (Fig. 1(e)). The broadening remains symmetric around the unstrained emission, indicating that high RF powers can be applied without inducing local heating of the QD. A good mechanical contact between the NW and the substrate is also maintained as the detuning does not drop even at high RF powers. However, the integrated lineshape decrease for all peaks slightly above 5 dBm (see Supporting Information Fig. S2). The next experiments were carried out below this threshold.

Time-resolved measurements were then performed to observe the strain tuning over one acoustic cycle. As drawn in Fig. 1(b), the PL signal was filtered by a monochromator (0.1 nm bandwidth) around the T_A emission line, detected by superconducting nanowire single photon detectors (time jitter around 20 ps) and counted by a time tagging device (time jitter below 10 ps) phase-locked to the signal generator. The sample was continuously excited with a He-Ne laser. A balanced power splitter was inserted at the output of the signal generator set at 247.5 MHz with output power 8 dBm. Half of the power triggered the counting module while the other half drove the IDT. Over an acoustic cycle, pulses in the count rate can be observed as soon as the T_A emission wavelength falls within the filtering bandwidth of the monochromator. By sweeping the filtering window across the strain-tuned emission line, the time-dependent modulation can be reconstructed as shown in Fig. 2(a). This modulation is sinusoidal with a fitted frequency of 247.64 MHz, which closely matches the RF drive frequency. The absence of distortions in the sine wave shows that the tuning is only induced by the deformation potential, without contribution from the piezoelectric field via the quantum confined Stark effect [47]. The purity of the single photon source was then assessed by measuring the second-order correlation function of the T_A line in a Hanbury Brown-Twiss measurement (Fig. 2(b)). The QD was continuously excited non-resonantly with a He-Ne laser. Without strain-tuning, $g^{(2)}(0) = 0.058$ is measured experimentally, whereas a value of 0.0313 ± 0.019 is found by fitting the data to a biexponential decay function, hence demonstrating the high purity of the emitter. A SAW was then generated at $P_{RF} = 4 \text{ dBm}$ while the PL was filtered at 846.58 nm, which corresponds to the wavelength where the modulation is maximum. Pulses were measured with a period of 4.039 ns and the peak

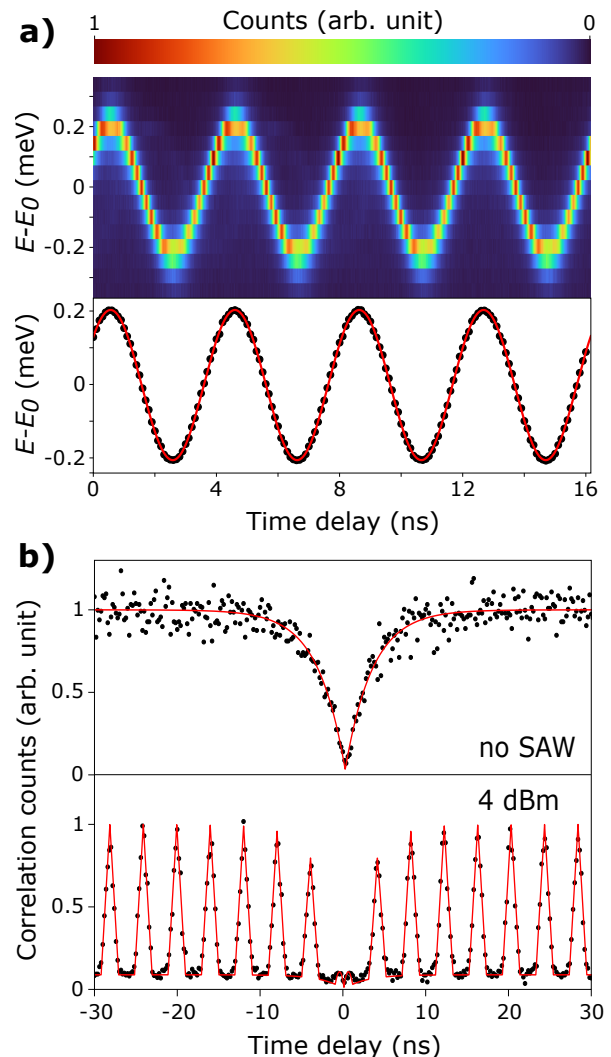


FIG. 2. a) PL spectra of the T_A line measured over 4 acoustic periods (top). The modulation with respect to the unstrained energy E_0 was extracted and fitted by a sine function (bottom) with a period of 4.038 ns. b) Second order correlation function of the T_A line without (top) and with (bottom) SAW interaction. In the latter case, the monochromator filtered at the energy corresponding to the maximum of the sine wave shown in a). The fitting function (red lines) are detailed in the main text. For all the measurements, the QD was continuously excited with a HeNe laser at 150 nW.

at zero time delay was strongly suppressed. The experimental data were fit based on the detection probability model introduced by Gell *et al.* [48] in which $g^{(2)}(\tau) = P_e(\tau)P_d(\tau)$, where $P_e(\tau)$ is the probability of the QD emitting a pair of photons with a temporal separation of τ (biexponential decay function), and $P_d(\tau)$ is the pair-detection probability (convolution of two trains of top hat functions). The experimental point at zero delay $g^{(2)}(0) = 0.042$ and the fitting parameter 0.0114 ± 0.026 are very similar to the values obtained without modulation. This measurement under continuous wave excitation demonstrates the pulsed genera-

tion of high purity single photons over the tuning range induced by the strain modulation. A similar measurement was carried out when the monochromator filtered at 846.2 nm (Supporting Information Fig. S3), and shows that the period of the pulses is divided by two since the modulated emission falls within the monochromator band pass twice over one acoustic cycle.

Next, the tuning of the QD emission was investigated after depositing a 320 nm-thick layer of SiO_2 by PECVD on the chip. The oxide on top of the IDTs was locally removed to have the same resonance frequency and the same electrical to acoustic transduction as previously (see Supporting Information Fig. S4 for a comparison of the scattering parameters). This oxide layer bonds the NW on the substrate more rigidly than the Van der Waals forces which provides two benefits. On the one hand, it eases the fabrication of subsequent photonic structures, and on the other hand, it plays the role of a cladding layer when the NW is integrated with a lithium niobate on insulator (LNOI) waveguide. The impact of this encapsulating layer on the acousto-optical coupling was analyzed by 2D FEM simulations with COMSOL in frequency domain. The SAW was excited at the fundamental resonance of a bulk 128° Y-X cut LiNbO_3 substrate, and propagated along the X-axis towards a NW modeled as a linear elastic slab of InP (thickness 100 nm) placed on top of the substrate. A linear elastic SiO_2 layer of variable thickness was added on top of this slab. The induced hydrostatic pressure [49] was computed at the center of the InP layer. The inset of Fig. 3 shows that the SiO_2 encapsulation improves the mechanical coupling between the SAW and the InP. For an oxide thickness of 320 nm, the hydrostatic pressure at the center of the InP layer is expected to increase by approximately 4%.

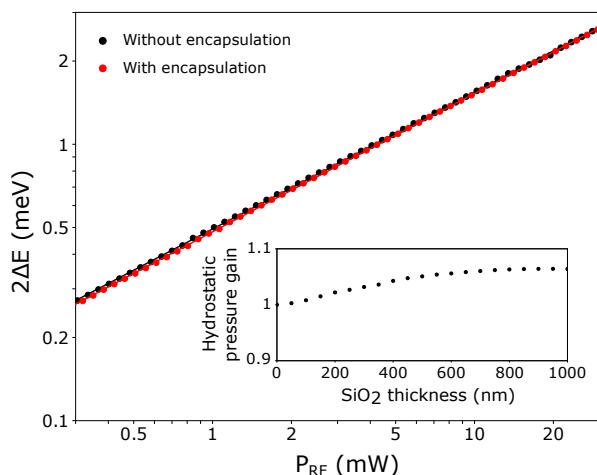


FIG. 3. Strain-induced energy splitting of the T_A line as a function of P_{RF} (log scale representation). The black and red points were taken before and after the deposition of SiO_2 (320 nm) on top of the NW, respectively. The solid lines are linear fits. In both cases, the excitation power was 150 nW. The inset shows the simulated hydrostatic pressure gain after the deposition of a SiO_2 layer on top of the InP/ LiNbO_3 stack.

To experimentally confirm the above simulation results, the energy broadening as a function of RF power (similar to Fig. 1(c)) was measured after the deposition of a 320 nm-thick layer of SiO_2 . The thickness was confirmed by profilometry. The driving frequency chosen to maximize the acousto-optical coupling was still 247.5 MHz. Independent of the SAW power, the PL lines were blueshifted by 1.92 nm, indicating a static strain introduced by the SiO_2 layer onto the QD. Without the SAW, no significant broadening of the QD emission line could be resolved after encapsulation. The optomechanical modulation amplitude $2\Delta E$ was extracted from the data by fitting to a time-integrated oscillating Lorentzian emission line [50]. The optomechanical response $2\Delta E$ is plotted as a function of the driving RF power in logarithmic scale before and after SiO_2 encapsulation (Fig. 3). In both cases, the strain-induced broadening follows the power law $2\Delta E \propto (P_{RF})^\alpha$, where $\alpha = 0.5001 \pm 0.0003$ with SiO_2 and $\alpha = 0.4951 \pm 0.0004$ without. These two coefficients are very close to the ideal value $\alpha = 0.5$ for a deformation potential coupling [51], demonstrating that the observed broadening is essentially due to optomechanical coupling. For a given RF power within the range -5 dBm to 15 dBm, the encapsulation resulted on average in a broadening smaller by around 1.8%. Assuming this decrease is only due to a lower hydrostatic pressure, this value is below the 4% enhancement obtained from the simulation. However, the discrepancy remains small and supports the idea that the encapsulation does not dramatically hinder the acousto-optical coupling.

Guiding the light emitted by the QD and modulated by SAWs would enable on-chip single photon manipulation and detection. Towards this direction, we propose a novel architecture shown in Fig. 4. The tapered NW is placed on top of an X-oriented rib waveguide made from a 400 nm-thick Y-cut LiNbO_3 on a Si/ SiO_2 wafer. The NW is modeled as a 10 μm -long truncated cone with base diameter 200 nm and top diameter 50 nm. The rib waveguide has a height of 200 nm, leaving a base of 200 nm to excite SAWs. The IDTs are parallel to the Z-axis of the crystal which has the largest electromechanical coupling coefficient. A thick buried oxide (3 μm) can be used to efficiently confine the optical mode in the rib waveguide. The tapered shape of the NW favors an adiabatic mode transfer of the TE and TM modes of the NW [14] to the fundamental TE and TM modes of the waveguide, respectively. Finite-difference time-domain simulations (Lumerical) were conducted to calculate the coupling efficiency of the device assuming lossless materials. For a 800 nm-wide rib waveguide, a coupling efficiency of 95.1% for the TE modes and 98% for the TM modes was obtained. This large waveguide geometry further facilitates the placement of the NW using a manipulator. The efficiency of other waveguide geometries can be found in Supporting Information Fig. S5.

The properties of the surface acoustic wave depends on their propagation medium. For the device under consideration, the Rayleigh wave phase velocity v_p and the

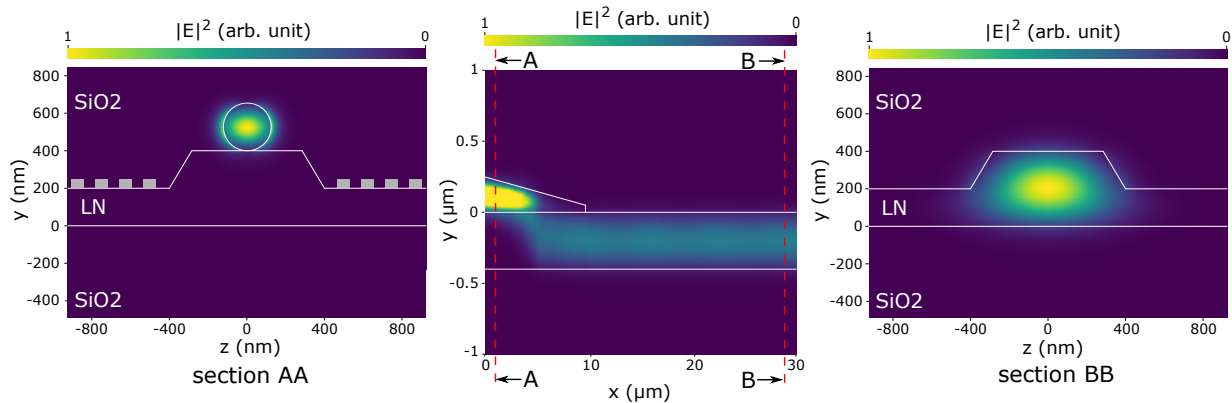


FIG. 4. Optical TE mode transfer between the tapered NW and the rib waveguide made from LiNbO₃ on SiO₂ (central figure). The device is covered by SiO₂ for cladding. The cross section AA (left image) shows the confined optical mode in the NW before the mode transfer region. The grey squares represent the electrodes of the two IDTs forming the delay line. The cross section BB (right image) represents the optical mode confined in the rib waveguide after the mode transfer region. The refractive indices at 850 nm are: $n_{\text{LiNbO}_3(e)} = 2.17$ - $n_{\text{LiNbO}_3(o)} = 2.25$ - $n_{\text{SiO}_2} = 1.45$ - $n_{\text{InP}} = 3.46$. The axes correspond to that of a Y-cut LNOI.

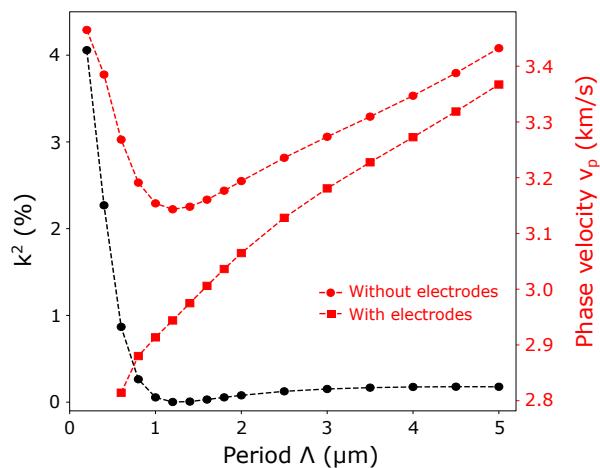


FIG. 5. Influence of the IDT period Λ on the electromechanical coefficient k^2 (black) and the Rayleigh wave phase velocity v_p (red) for Y-Z LNOI (200 nm LiNbO₃ - 3 μm SiO₂).

electromechanical coupling coefficient k^2 now depend on the thicknesses of the LiNbO₃ and SiO₂ layers. These two parameters were assessed by 2D FEM simulations with COMSOL in eigenmode. Two electrodes (60 nm of chromium) are present on the surface of the modeled LiNbO₃/SiO₂/Si layer stack. By grounding one electrode while setting the other to a floating potential, two propagating modes, one symmetric and one anti-symmetric, are identified. The Rayleigh wave phase velocity is derived as $v_p = (f_S + f_A) \cdot \Lambda/2$, where f_S and f_A are the frequencies of the symmetric and anti-symmetric modes, respectively. The electromechanical coupling coefficient is computed as $k^2 = 2(v_{p,o} - v_{p,s})/v_{p,o}$, where $v_{p,o}$ and $v_{p,s}$ are the phase velocity when the surface is open and shorted, respectively [52]. For 200 nm LiNbO₃ and 3 μm buried SiO₂, the influence of the IDT period is shown

in Fig. 5. For a period comparable to the LiNbO₃ thickness, the coefficient k^2 converges to the bulk value around 4.1%. Similar optomechanical coupling as demonstrated above is therefore expected. The phase velocity converges to the phase velocity of bulk LiNbO₃ around 3490 ms^{-1} when no physical electrodes are on the surface. Adding the electrodes slows down the wave drastically due to their weight, and the modes are distorted for very short periods. Up to $\Lambda < 1 \mu\text{m}$, the wave mainly propagates in the LiNbO₃ film and partially leaks in the SiO₂ layer, which results in lower velocity and a drastic decline of the coefficient k^2 . For $\Lambda > 1 \mu\text{m}$, the phase velocity increases as the wave penetrates deeper in the SiO₂ to reach the Si substrate which is faster medium than SiO₂ and LiNbO₃. The coefficient k^2 also increases to converge to a value of 0.17% due to the waveguiding effect in the LiNbO₃ and SiO₂ layers, which couples more vibration in these layers. This value of k^2 , although smaller by an order of magnitude than the bulk scenario, is still larger than bulk GaAs ($\approx 0.07\%$) on which modulation of In(Ga)As QDs has been demonstrated [53]. Therefore, this LNOI platform is a compelling approach for strain modulation of integrated QDs nanowires.

In conclusion, we demonstrated the dynamic modulation of the emission of a quantum dot nanowire, transferred to a LiNbO₃ substrate, using surface acoustic waves. The strong optomechanical coupling results in a wide optical tuning range at moderate RF powers, thereby avoiding heating of the sample, charge transport or Stark effect modulation. The purity of the single photon source was preserved during the dynamic modulation process. Adding a SiO₂ encapsulation layer on top of the nanowire does not significantly deteriorate the modulation and presents two benefits. It firmly anchors the nanowire to the substrate and acts as a cladding layer when the nanowire is integrated on a waveguide. Towards this idea, we proposed an architecture to adiabatic-

ically transfer the light emitted by the quantum dot into a rib waveguide made from LNOI compatible with strain modulation. Optimal optomechanical coupling will be obtained when the SAW period is comparable to the LiNbO_3 thickness. Larger period will result in weaker optomechanical coupling, but the performance can be further enhanced by patterning acoustic Bragg mirrors around the delay line and placing the QD in the nanowire at the anti-nodes of the SAW resonator [45]. In addition to the source modulation, the properties of other photonic components such as Mach-Zehnder interferometers and ring resonators can also be acoustically modulated to engineer reconfigurable quantum photonic circuits on

LNOI.

ACKNOWLEDGMENTS

The work was partially supported by the Knut and Alice Wallenberg (KAW) Foundation through the Wallenberg Centre for Quantum Technology (WACQT) and the SSF funding for the Sweden Taiwan collaboration. The authors also acknowledge the support from the European Union's Horizon 2020 Research and Innovation Programme through the project aCryComm, FET Open Grant Agreement no. 899558.

-
- [1] J. L. O'Brien, Optical quantum computing, *Science* **318**, 1567 (2007).
- [2] H. S. Zhong, H. Wang, Y. H. Deng, M. C. Chen, L. C. Peng, Y. H. Luo, J. Qin, D. Wu, X. Ding, Y. Hu, P. Hu, X. Y. Yang, W. J. Zhang, H. Li, Y. Li, X. Jiang, L. Gan, G. Yang, L. You, Z. Wang, L. Li, N. L. Liu, C. Y. Lu, and J. W. Pan, Quantum computational advantage using photons, *Science* **370**, 1460 (2020).
- [3] A. W. Elshaari, W. Pernice, K. Srinivasan, O. Benson, and V. Zwiller, Hybrid integrated quantum photonic circuits, *Nature Photonics* **14**, 285 (2020).
- [4] E. Pelucchi, G. Fagas, I. Aharonovich, D. Englund, E. Figueroa, Q. Gong, H. Hannes, J. Liu, C. Y. Lu, N. Matsuda, J. W. Pan, F. Schreck, F. Sciarrino, C. Silberhorn, J. Wang, and K. D. Jöns, The potential and global outlook of integrated photonics for quantum technologies, *Nature Reviews Physics* **4**, 194 (2022).
- [5] S. Bounouar, M. Davanco, and S. Reitzenstein, Quantum integrated photonic circuits, *Semiconductors and Semimetals* **105**, 153 (2020).
- [6] S. Rodt and S. Reitzenstein, Integrated nanophotonics for the development of fully functional quantum circuits based on on-demand single-photon emitters, *APL Photonics* **6**, 010901 (2021).
- [7] G. Moody, V. J. Sorger, D. J. Blumenthal, P. W. Juodawlkis, W. Loh, C. Sorace-Agaskar, A. E. Jones, K. C. Balram, J. C. Matthews, A. Laing, M. Davanco, L. Chang, J. E. Bowers, N. Quack, C. Galland, I. Aharonovich, M. A. Wolff, C. Schuck, N. Sinclair, M. Lončar, T. Komljenovic, D. Weld, S. Mookherjee, S. Buckley, M. Radulaski, S. Reitzenstein, B. Pingault, B. Machielse, D. Mukhopadhyay, A. Akimov, A. Zheltikov, G. S. Agarwal, K. Srinivasan, J. Lu, H. X. Tang, W. Jiang, T. P. McKenna, A. H. Safavi-Naeini, S. Steinhauer, A. W. Elshaari, V. Zwiller, P. S. Davids, N. Martinez, M. Gehl, J. Chiaverini, K. K. Mehta, J. Romero, N. B. Lingaraju, A. M. Weiner, D. Peace, R. Cernansky, M. Lobino, E. Diamanti, L. T. Vidarte, and R. M. Camacho, 2022 Roadmap on integrated quantum photonics, *JPhys Photonics* **4**, 012501 (2022).
- [8] C. P. Dietrich, A. Fiore, M. G. Thompson, M. Kamp, and S. Höfling, GaAs integrated quantum photonics: Towards compact and multi-functional quantum photonic integrated circuits, *Laser & Photonics Reviews* **10**, 870 (2016).
- [9] F. Lenzi, N. Gruhler, N. Walter, and W. H. Pernice, Diamond as a Platform for Integrated Quantum Photonics, *Advanced Quantum Technologies* **1**, 1800061 (2018).
- [10] A. Chanana, H. Larocque, R. Moreira, J. Carolan, B. Guha, E. G. Melo, V. Anant, J. Song, D. Englund, D. J. Blumenthal, K. Srinivasan, and M. Davanco, Ultra-low loss quantum photonic circuits integrated with single quantum emitters, *Nature Communications* **13**, 1 (2022).
- [11] S. Aghaieimeibodi, B. Desiatov, J. H. Kim, C. M. Lee, M. A. Buyukkaya, A. Karasahin, C. J. Richardson, R. P. Leavitt, M. Lončar, and E. Waks, Integration of quantum dots with lithium niobate photonics, *Applied Physics Letters* **113**, 221102 (2018).
- [12] R. Katsumi, Y. Ota, T. Tajiri, M. Kakuda, S. Iwamoto, H. Akiyama, and Y. Arakawa, Unidirectional output from a quantum-dot single-photon source hybrid integrated on silicon, *Optics Express* **29**, 37117 (2021).
- [13] A. W. Elshaari, I. E. Zadeh, A. Fognini, M. E. Reimer, D. Dalacu, P. J. Poole, V. Zwiller, and K. D. Jöns, On-chip single photon filtering and multiplexing in hybrid quantum photonic circuits, *Nature Communications* **8**, 1 (2017).
- [14] K. Mnaymneh, D. Dalacu, J. McKee, J. Lapointe, S. Haffouz, J. F. Weber, D. B. Northeast, P. J. Poole, G. C. Aers, R. L. Williams, K. Mnaymneh, D. Dalacu, J. McKee, J. Lapointe, S. Haffouz, J. F. Weber, D. B. Northeast, P. J. Poole, G. C. Aers, and R. L. Williams, On-Chip Integration of Single Photon Sources via Evanescent Coupling of Tapered Nanowires to SiN Waveguides, *Advanced Quantum Technologies* **3**, 1900021 (2020).
- [15] N. H. Wan, T. J. Lu, K. C. Chen, M. P. Walsh, M. E. Trusheim, L. De Santis, E. A. Bersin, I. B. Harris, S. L. Mouradian, I. R. Christen, E. S. Bielejec, and D. Englund, Large-scale integration of artificial atoms in hybrid photonic circuits, *Nature* **583**, 226 (2020).
- [16] X. Guo, N. Deegan, J. C. Karsch, Z. Li, T. Liu, R. Shreiner, A. Butcher, D. D. Awschalom, F. J. Heremans, and A. A. High, Tunable and Transferable Diamond Membranes for Integrated Quantum Technologies, *Nano Letters* **21**, 10392 (2021).
- [17] D. White, A. Branny, R. J. Chapman, R. Picard, M. Brotons-Gisbert, A. Boes, A. Peruzzo, C. Bonato, and B. D. Gerardot, Atomically-thin quantum dots integrated with lithium niobate photonic chips [Invited], *Optical Materials Express* **9**, 441 (2019).

- [18] F. Peyskens, C. Chakraborty, M. Muneeb, D. Van Thourhout, and D. Englund, Integration of single photon emitters in 2D layered materials with a silicon nitride photonic chip, *Nature Communications* **10**, 1 (2019).
- [19] X.-J. Liu, Y. Yu, D. Liu, Q.-L. Cui, X. Qi, Y. Chen, G. Qu, L. Song, G.-P. Guo, G.-C. Guo, X. Sun, and X.-F. Ren, Coupling of Photon Emitters in Monolayer WS₂ with a Photonic Waveguide Based on Bound States in the Continuum, *Nano Letters* **23**, 3209 (2023).
- [20] R. Trotta, P. Atkinson, J. D. Plumhof, E. Zallo, R. O. Rezaev, S. Kumar, S. Baunack, J. R. Schröter, A. Rastelli, and O. G. Schmidt, Nanomembrane quantum-light-emitting diodes integrated onto piezoelectric actuators, *Advanced Materials* **24**, 2668 (2012).
- [21] M. Bayer, G. Ortner, O. Stern, A. Kuther, A. A. Gorbunov, A. Forchel, P. Hawrylak, S. Fafard, K. Hinzer, T. L. Reinecke, S. N. Walck, J. P. Reithmaier, F. Klopff, and F. Schäfer, Fine structure of neutral and charged excitons in self-assembled In(Ga)As/(Al)GaAs quantum dots, *Physical Review B* **65**, 195315 (2002).
- [22] J. Martín-Sánchez, R. Trotta, A. Mariscal, R. Serna, G. Piredda, S. Stroj, J. Edlinger, C. Schimpf, J. Aberl, T. Lettner, J. Wildmann, H. Huang, X. Yuan, D. Ziss, J. Stangl, and A. Rastelli, Strain-tuning of the optical properties of semiconductor nanomaterials by integration onto piezoelectric actuators, *Semiconductor Science and Technology* **33**, 013001 (2017).
- [23] J. Zhang, J. S. Wildmann, F. Ding, R. Trotta, Y. Huo, E. Zallo, D. Huber, A. Rastelli, and O. G. Schmidt, High yield and ultrafast sources of electrically triggered entangled-photon pairs based on strain-tunable quantum dots, *Nature Communications* **6**, 1 (2015).
- [24] Dumur, K. J. Satzinger, G. A. Peairs, M. H. Chou, A. Bienfait, H. S. Chang, C. R. Conner, J. Grebel, R. G. Povey, Y. P. Zhong, and A. N. Cleland, Quantum communication with itinerant surface acoustic wave phonons, *npj Quantum Information* **7**, 1 (2021).
- [25] A. Bienfait, K. J. Satzinger, Y. P. Zhong, H. S. Chang, M. H. Chou, C. R. Conner, Dumur, J. Grebel, G. A. Peairs, R. G. Povey, and A. N. Cleland, Phonon-mediated quantum state transfer and remote qubit entanglement, *Science* **364**, 368 (2019).
- [26] B. Jadot, P. A. Mortemousque, E. Chanrion, V. Thiney, A. Ludwig, A. D. Wieck, M. Urdampilleta, C. Bäuerle, and T. Meunier, Distant spin entanglement via fast and coherent electron shuttling, *Nature Nanotechnology* **16**, 570 (2021).
- [27] P. Imany, Z. Wang, R. A. DeCrescent, R. C. Boutelle, C. A. McDonald, T. Autry, S. Berweger, P. Kabos, S. W. Nam, R. P. Mirin, and K. L. Silverman, Quantum phase modulation with acoustic cavities and quantum dots, *Optica* **9**, 501 (2022).
- [28] M. Weiß, D. Wigger, M. Nägele, K. Müller, J. J. Finley, T. Kuhn, P. Machnikowski, and H. J. Krenner, Optomechanical wave mixing by a single quantum dot, *Optica* **8**, 291 (2021).
- [29] A. Hernández-Mínguez, M. Möller, S. Breuer, C. Pfüller, C. Somaschini, S. Lazić, O. Brandt, A. García-Cristóbal, M. M. De Lima, A. Cantarero, L. Geelhaar, H. Riechert, and P. V. Santos, Acoustically driven photon antibunching in nanowires, *Nano Letters* **12**, 252 (2012).
- [30] B. Villa, A. J. Bennett, D. J. Ellis, J. P. Lee, J. Skiba-Szymanska, T. A. Mitchell, J. P. Griffiths, I. Farrer, D. A. Ritchie, C. J. Ford, and A. J. Shields, Surface acoustic wave modulation of a coherently driven quantum dot in a pillar microcavity, *Applied Physics Letters* **111**, 011103 (2017).
- [31] V. Tiwari, K. Makita, M. Arino, M. Morita, T. Crozes, E. Bellet-Amalric, S. Kuroda, H. Boukari, and L. Besombes, Radio-frequency stress-induced modulation of CdTe/ZnTe quantum dots, *Journal of Applied Physics* **127**, 234303 (2020).
- [32] S. Lazić, A. Espinha, S. Pinilla Yanguas, C. Gibaja, F. Zamora, P. Ares, M. Chhowalla, W. S. Paz, J. J. P. Burgos, A. Hernández-Mínguez, P. V. Santos, and H. P. van der Meulen, Dynamically tuned non-classical light emission from atomic defects in hexagonal boron nitride, *Communications Physics* **2**, 1 (2019).
- [33] D. D. Bühler, M. Weiß, A. Crespo-Poveda, E. D. Nysten, J. J. Finley, K. Müller, P. V. Santos, M. M. de Lima, and H. J. Krenner, On-chip generation and dynamic piezomechanical rotation of single photons, *Nature Communications* **13**, 1 (2022).
- [34] J. Chang, J. Gao, I. Esmaeil Zadeh, A. W. Elshaari, and V. Zwiller, Nanowire-based integrated photonics for quantum information and quantum sensing, *Nanophotonics* **12**, 339 (2023).
- [35] J. Gao, L. Santos, G. Krishna, Z.-S. Xu, A. Iovan, S. Steinhauer, O. Gühne, P. J. Poole, D. Dalacu, V. Zwiller, and A. W. Elshaari, Scalable Generation and Detection of on-Demand W States in Nanophotonic Circuits, *Nano Letters* 10.1021/ACS.NANOLETT.3C01551 (2023).
- [36] M. E. Reimer, G. Bulgarini, N. Akopian, M. Hocevar, M. B. Bavinck, M. A. Verheijen, E. P. Bakkers, L. P. Kouwenhoven, and V. Zwiller, Bright single-photon sources in bottom-up tailored nanowires, *Nature Communications* **3**, 1 (2012).
- [37] D. Dalacu, K. Mnaymneh, J. Lapointe, X. Wu, P. J. Poole, G. Bulgarini, V. Zwiller, and M. E. Reimer, Ultra-clean emission from InAsP quantum dots in defect-free wurtzite InP nanowires, *Nano Letters* **12**, 5919 (2012).
- [38] P. Laferrière, A. Yin, E. Yeung, L. Kusmic, M. Korkusinski, P. Rasekh, D. B. Northeast, S. Haffouz, J. Lapointe, P. J. Poole, R. L. Williams, and D. Dalacu, Approaching transform-limited photons from nanowire quantum dots using excitation above the band gap, *Physical Review B* **107**, 155422 (2023).
- [39] M. A. Versteegh, M. E. Reimer, K. D. Jöns, D. Dalacu, P. J. Poole, A. Gulinatti, A. Giudice, and V. Zwiller, Observation of strongly entangled photon pairs from a nanowire quantum dot, *Nature Communications* **5**, 1 (2014).
- [40] K. D. Jöns, L. Schweickert, M. A. Versteegh, D. Dalacu, P. J. Poole, A. Gulinatti, A. Giudice, V. Zwiller, and M. E. Reimer, Bright nanoscale source of deterministic entangled photon pairs violating Bell's inequality, *Scientific Reports* **7**, 1 (2017).
- [41] P. Laferrière, E. Yeung, I. Miron, D. B. Northeast, S. Haffouz, J. Lapointe, M. Korkusinski, P. J. Poole, R. L. Williams, and D. Dalacu, Unity yield of deterministically positioned quantum dot single photon sources, *Scientific Reports* **12**, 1 (2022).
- [42] A. W. Elshaari, E. Büyüközer, I. E. Zadeh, T. Lettner, P. Zhao, E. Schöll, S. Gyger, M. E. Reimer, D. Dalacu, P. J. Poole, K. D. Jöns, and V. Zwiller, Strain-Tunable Quantum Integrated Photonics, *Nano Letters* **18**, 7969 (2018).

- [43] I. E. Zadeh, A. W. Elshaari, K. D. Jöns, A. Fognini, D. Dalacu, P. J. Poole, M. E. Reimer, and V. Zwiller, Deterministic Integration of Single Photon Sources in Silicon Based Photonic Circuits, *Nano Letters* **16**, 2289 (2016).
- [44] R. Gourgues, I. E. Zadeh, A. W. Elshaari, G. Bulgarelli, J. W. N. Los, J. Zichi, D. Dalacu, P. J. Poole, S. N. Dorenbos, and V. Zwiller, Controlled integration of selected detectors and emitters in photonic integrated circuits, *Optics Express* **27**, 3710 (2019), arXiv:1811.03979.
- [45] E. D. Nysten, Y. H. Huo, H. Yu, G. F. Song, A. Rastelli, and H. J. Krenner, Multi-harmonic quantum dot optomechanics in fused LiNbO₃-(Al)GaAs hybrids, *Journal of Physics D: Applied Physics* **50**, 43LT01 (2017).
- [46] A. A. M. Ralib, A. N. Nordin, A. Z. Alam, U. Hashim, and R. Othman, Piezoelectric thin films for double electrode CMOS MEMS surface acoustic wave (SAW) resonator, *Microsystem Technologies* **21**, 1931 (2015).
- [47] M. Weiß, F. J. Schüle, J. B. Kinzel, M. Heigl, D. Rudolph, M. Bichler, G. Abstreiter, J. J. Finley, A. Wixforth, G. Koblmüller, and H. J. Krenner, Radio frequency occupancy state control of a single nanowire quantum dot, *Journal of Physics D: Applied Physics* **47**, 394011 (2014).
- [48] J. R. Gell, M. B. Ward, R. J. Young, R. M. Stevenson, P. Atkinson, D. Anderson, G. A. Jones, D. A. Ritchie, and A. J. Shields, Modulation of single quantum dot energy levels by a surface-acoustic-wave, *Applied Physics Letters* **93**, 10.1063/1.2976135 (2008).
- [49] M. Weiß and H. J. Krenner, Interfacing quantum emitters with propagating surface acoustic waves, *Journal of Physics D: Applied Physics* **51**, 373001 (2018).
- [50] E. D. Nysten, A. Rastelli, and H. J. Krenner, A hybrid (Al)GaAs-LiNbO₃ surface acoustic wave resonator for cavity quantum dot optomechanics, *Applied Physics Letters* **117**, 121106 (2020).
- [51] J. Pustowski, K. Müller, M. Bichler, G. Koblmüller, J. J. Finley, A. Wixforth, and H. J. Krenner, Independent dynamic acousto-mechanical and electrostatic control of individual quantum dots in a LiNbO₃-GaAs hybrid, *Applied Physics Letters* **106**, 13107 (2015).
- [52] U. C. Kaletta and C. Wenger, FEM simulation of Rayleigh waves for CMOS compatible SAW devices based on AlN/SiO₂/Si(1 0 0), *Ultrasonics* **54**, 291 (2014).
- [53] M. Weiß, A. L. Hörner, E. Zallo, P. Atkinson, A. Rastelli, O. G. Schmidt, A. Wixforth, and H. J. Krenner, Multiharmonic Frequency-Chirped Transducers for Surface-Acoustic-Wave Optomechanics, *Physical Review Applied* **9**, 014004 (2018).

Supporting Information

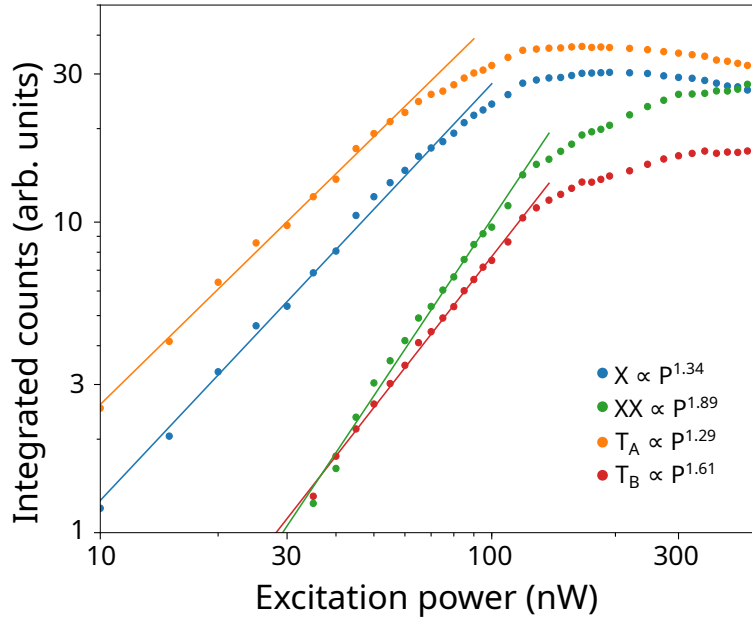


FIG. S1. Power dependent measurement of the four emission lines identified in the nanowire quantum dot excited with a HeNe laser. The points are experimental values and the solid lines linear fits. The blue, green, orange and red data sets correspond to the lines labeled X , XX , T_A , T_B in the main text, respectively. X and T_A exhibit the lowest slopes while XX and T_B have the greatest ones

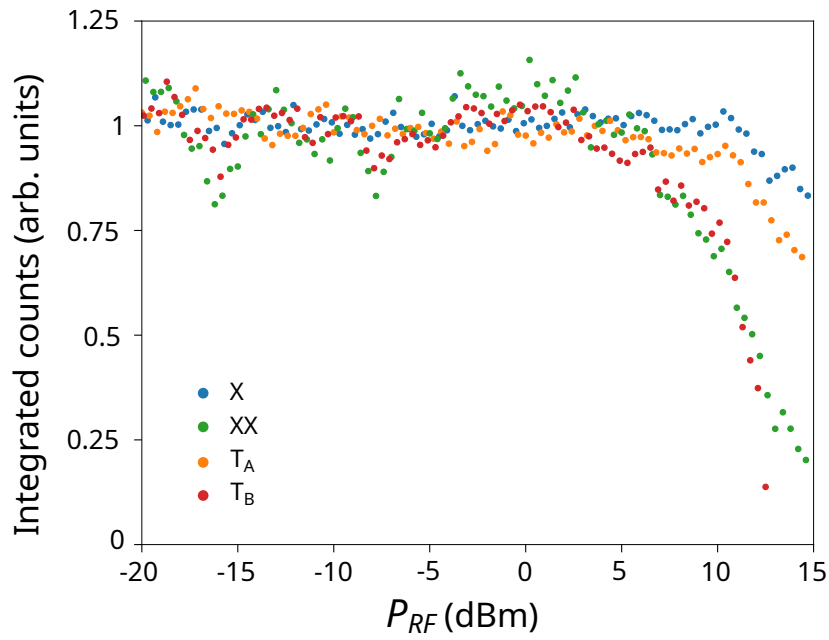


FIG. S2. Integrated count rates of the four peaks represented in Fig. 1(e) in the main text. Each peak was fitted by a time-integrated oscillating Lorentzian. The intensity starts to drop for all the peaks slightly above $P_{RF} = 5$ dBm. Heating of the QD does not seem to be the reason since no global redshift of the broadened peaks is observed.

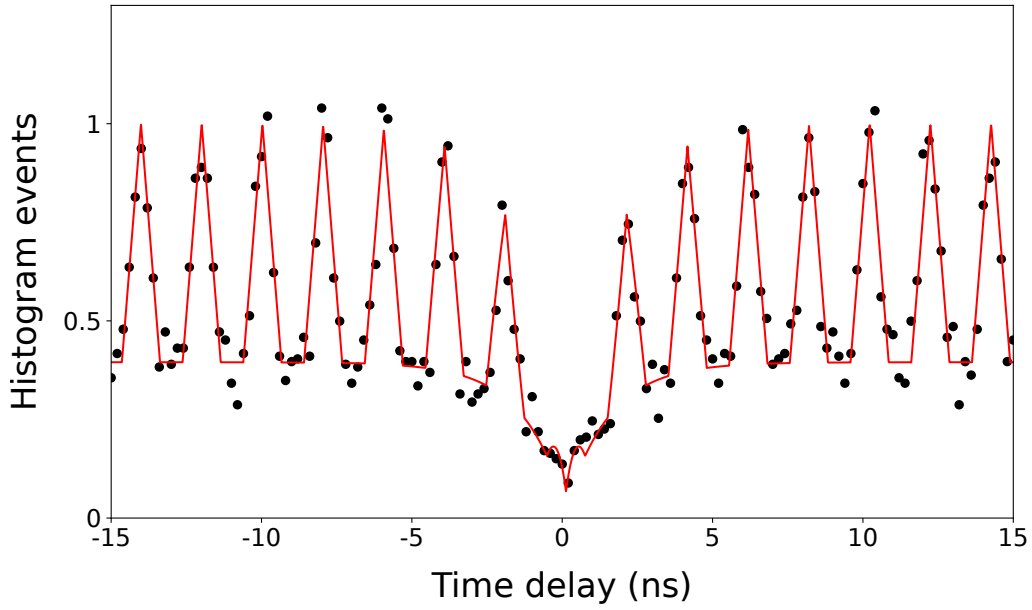


FIG. S3. Hanbury-Brown Twiss experiments of the T_A line when the SAW is generated at $P_{RF} = 4$ dBm and the monochromator set to 846.2 nm, corresponding to the wavelength where the acoustic field is minimum. The black dots are experimental values and the red curve is the fit based on the same function as described in the main text. The period of the pulses is 2.019 ns, which is half of the SAW period since the modulated T_A line falls in the band pass of the monochromator twice. The value $g^{(2)}(0) = 0.066$ is larger than the one shown in the main text, but can be improved with longer integration time.

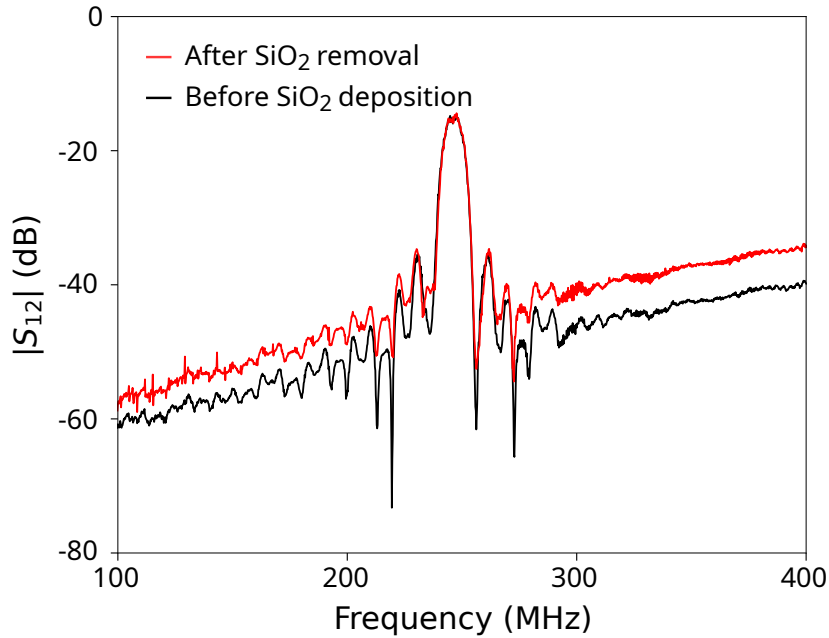


FIG. S4. Transmission spectrum of the delay line before oxide deposition (black) and after oxide removal on the IDT (red). The resonance peak at 245 MHz has the same linewidth and amplitude, showing that the device performance has not been affected by the process in this region. The background outside the resonance is higher by approximately 5 dB after oxide removal, but this change does not affect the device operation.

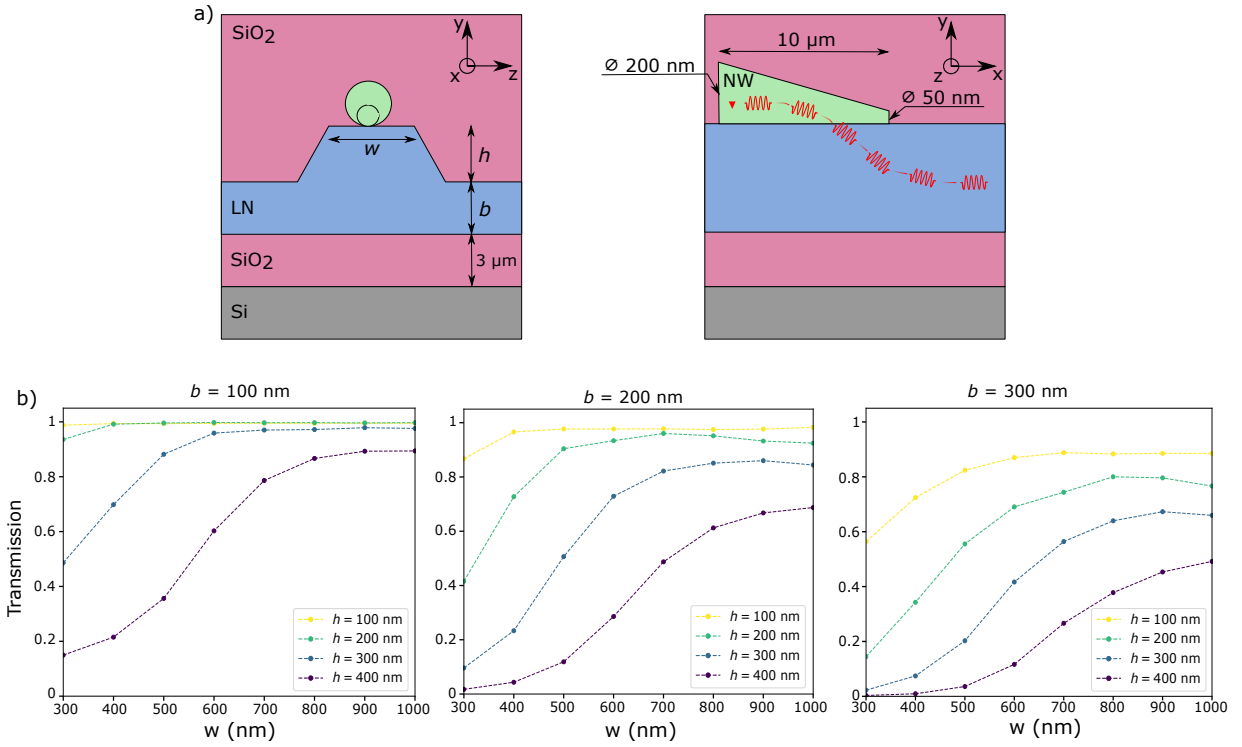


FIG. S5. Parametric study of the LNOI waveguide geometry based on Lumerical simulations using the EME solver. The input port (port 1) is set to the fundamental TE mode of the nanowire and the output port (port 2) is the fundamental TE mode of the LN waveguide. a) YZ view and YX view of the geometry and layer stack. All the materials are considered loss-less. b) The transmission, representing the coupling efficiency between the nanowire and the waveguide modes, is computed at 850 nm as a function of the waveguide width w , waveguide height h and base thickness b . Higher transmissions are obtained for waveguides with large cross section and small base thickness.

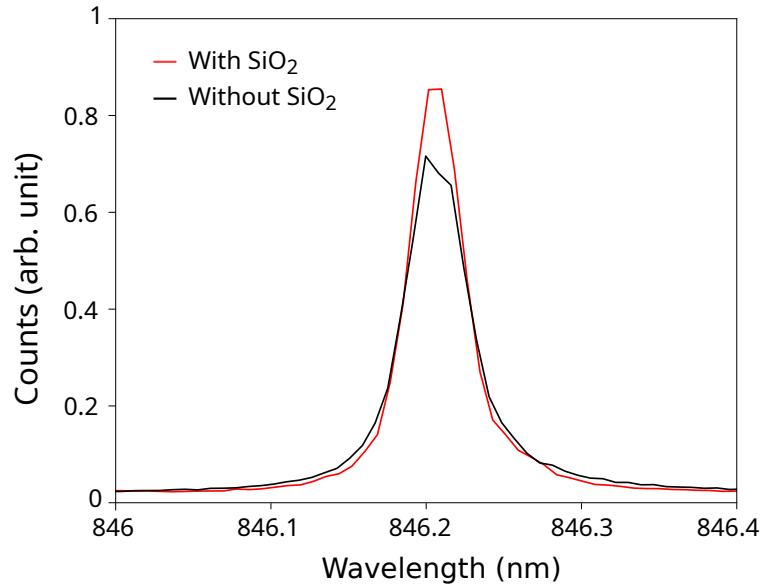


FIG. S6. Spectral linewidth of the T_A line before (black) and after (red) oxide deposition. The red curve has been shifted by 1.92 nm to compensate for the constant blueshift introduced by the oxide. No significant broadening could be observed. The quantum dot was excited continuously with a HeNe laser at 150 nW.

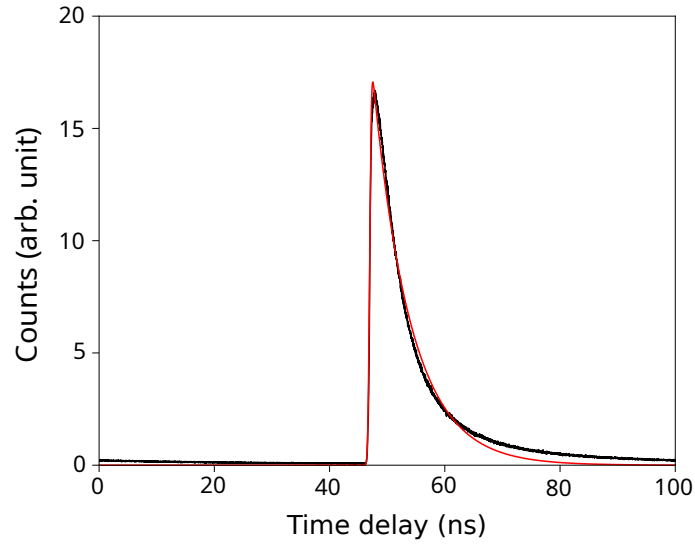


FIG. S7. Lifetime measurement (black line) of the T_A line. The experimental curve has been fitted by exponential decay function convoluted with the instrument response function (gaussian with a standard deviation of 244ps). The extracted lifetime is 6.52 ± 0.1 ns. The quantum dot was excited with a pulsed HeNe laser at 150 nW.

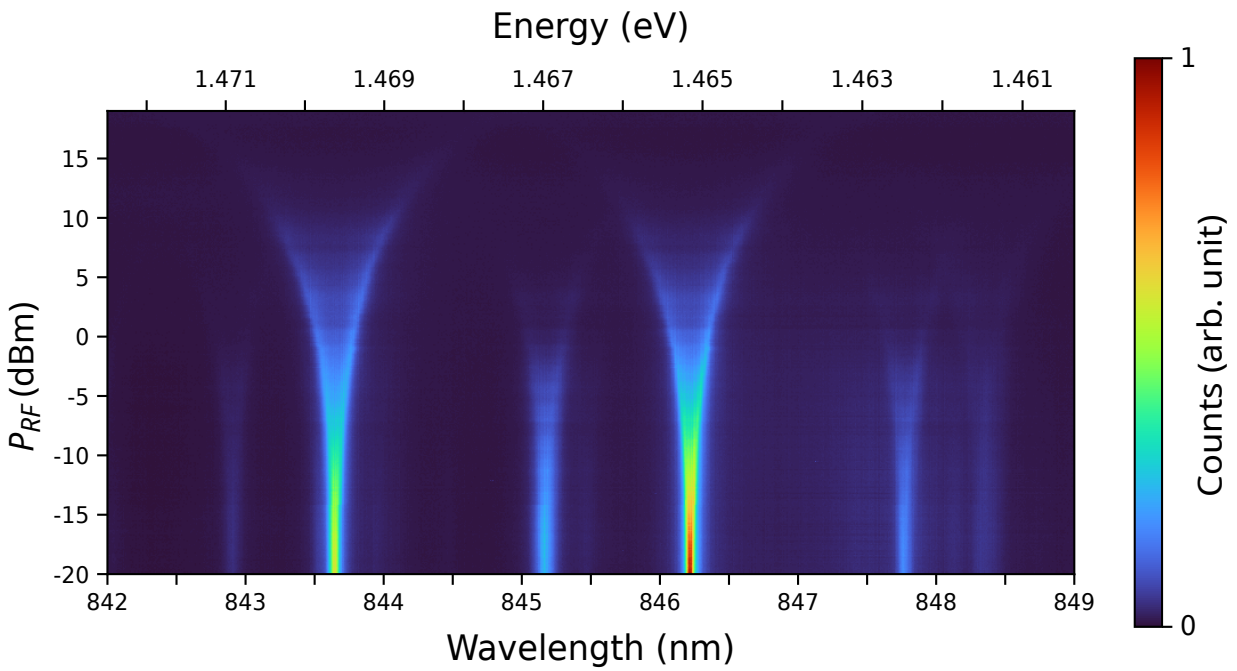


FIG. S8. Strain-induced energy broadening of the emission lines of the nanowire quantum dot by driving the IDT at the third harmonic 735 MHz. The nanowire QD shows a response similar to the modulation with the fundamental mode. The quantum dot was excited with a HeNe laser at 150 nW.